



Quantitative Analysis of Asymmetric Flux Reversal Permanent Magnet Linear Machine for Long Excursion Application

Yiming Shen Member, IEEE, Zhaokai Li Member, IEEE, Zhiqiang Zeng , Qinfen Lu Senior Member, IEEE, and Christopher H. T. Lee Senior Member, IEEE

Abstract—This article proposes two kinds of asymmetric flux reversal permanent magnet linear machine (AFR-PMLM) for long excursion application. By utilizing asymmetric permanent magnet excitation, the AFR-PMLM can effectively generate and fully exploit the second-order harmonic magnetomotive force (MMF), leading to a significant enhancement in thrust force density. First, the machine topology and operation principle are introduced. Then, the thrust force generation mechanism under multi MMFs is analytically calculated based on an improved MMF-permeance model, and further verified by finite element analysis. Various electromagnetic performances, including open-circuit characteristics, thrust force performances, and power factor, are comparatively studied. It shows that the proposed AFR-PMLM with consequent pole structure can provide 40.1% higher average force than conventional FR-PMLM under rated condition. In addition, it consumes only about 39.5% of the PMs volume while providing approximately 90.4% of the thrust force compared with switched flux PMLM. More importantly, the AFR-PMLM consumes only 1/80 PMs volume while achieving 75.0% of the thrust force density compared with conventional PMLM for a long excursion with 10 m. Finally, two prototypes of AFR-PMLM are manufactured for experimental validation.

Index Terms—Asymmetric excitation, flux reversal, linear machine, permanent magnet (PM), primary excitation.

I. INTRODUCTION

LINEAR machines can directly convey linear motion without any middle transmissions, which has been deeply investigated and widely used in transportation, industrial servo

Manuscript received 26 July 2023; revised 24 October 2023; accepted 6 December 2023. This work was supported in part by the National Research Foundation (NRF) Singapore through NRF Fellowship under Grant NRF-NRFF12-2020-0003 and in part by the National Natural Science Foundation of China under Grant 52107060 and Grant 52177061. (Corresponding author: Christopher H. T. Lee.)

Yiming Shen, Zhiqiang Zeng, and Christopher H. T. Lee are with the School of Electrical and Electronic Engineering, Nanyang Technological University, Singapore 639798 (e-mail: yiming.shen@ntu.edu.sg; zhiqiang.zeng@ntu.edu.sg; chtlee@ntu.edu.sg).

Zhaokai Li is with the KTH Royal Institute of Technology, 10044 Stockholm, Sweden (e-mail: zhaokai@kth.se).

Qinfen Lu is with the College of Electrical Engineering, Zhejiang University, Hangzhou 310027, China (e-mail: luqinfen@zju.edu.cn).

Color versions of one or more figures in this article are available at <https://doi.org/10.1109/TIE.2023.3344854>.

Digital Object Identifier 10.1109/TIE.2023.3344854

0278-0046 © 2024 IEEE. Personal use is permitted, but republication/redistribution requires IEEE permission.
See <https://www.ieee.org/publications/rights/index.html> for more information.

system, free-piston engine generator, and so on [1], [2], [3]. With the rapid development and great progress of rare-Earth permanent magnets (PMs), permanent magnet linear machine (PMLM) has been applied in more and more industrial applications with the merits of high force density, high precision, high dynamic response, and high reliability, referred to as “4 High.” Nevertheless, high performance always comes with high cost, especially the cost of rare-Earth PMs. Hence, increasing the thrust force density of PMLM with less usage of rare-Earth PMs has become a research hotspot in academia and industry.

For conventional PMLM, the secondary with PMs is always set as long stator and the primary with winding is set as short mover. Some of the researchers propose consequent pole (CP) structure to reduce half of the PMs usage in the long stator [4], [5], [6]. Moreover, the end force and force ripple can be greatly reduced by adopting modular mover structure. However, when applied to long excursion applications ranging from tens of meters to hundreds of meters, the PMs usage in the long stator becomes extremely high and the total cost of conventional PMLM cannot be effectively reduced. Hence, new types of PMLM with high-thrust force density and low cost are in urgent need for long excursion applications.

Over the past two decades, a new series of primary-excited PMLM (PE-PMLM) that concentrating both the armature winding and PMs in the short mover is proposed and has attracted more and more attention [7]. Different from the conventional PMLM, the secondary in PE-PMLM is free of PMs and only made of low-cost iron core. Therefore, PE-PMLM makes it possible to greatly reduce the consumption of rare-Earth PMs and thereby significantly cut down the total cost. According to the PMs position distribution in the primary, PE-PMLM can be divided into three main types, i.e., switched flux (SF-) PMLM, doubly salient (DS-) PMLM, and flux reversal (FR-) PMLM, and the details can be introduced as follows.

The key characteristic of SF-PMLM is that the PMs are sandwiched by the segmented primary cores to realize flux concentration effect. Many researchers try to improve the performance of SF-PMLM by adopting novel topologies. Lu et al. proposed multiteeth structure, partitioned-primary structure, and hybrid excitation to effectively improve the thrust force density [8], [9], [10], [11]. Cao et al. presented several types of modular structures to eliminate the harmonics and enhance the fault-tolerance capability [12], [13]. In addition, some advanced

control methods are also proposed by the authors in [14] and [15] to enhance the dynamic property as well as the fault-tolerant performance. Meanwhile, DS-PMLM also exhibits similar segmented structure as SF-PMLM. Some of the DS-PMLM insert the PMs in the primary yoke, while others insert the PMs in the primary slot with parallel excitation [16], [17]. Due to the saturation and low PMs utilization issues in above two kinds of machines, the overload capability and thrust force density of DS-PMLM are limited. In addition, since both SF-PMLM and DS-PMLM have segmented components in the primary, these two types of machines suffer from low mechanical reliability and complex assembly issue under the inevitable effect of large normal force that existing in single-sided PMLM. This limits the practical application to a certain extent.

In recent years, there has been increased attention toward flux reversal PM machines (FR-PMM) and their derived vernier structures, which have a high pole-pair number (PPN) of PMs excitation. This is primarily due to their simpler and more robust structure. The authors in [18], [19], and [20] deeply investigated the torque performance and brought CP structure into FR-PMM to reduce the PMs usage while enhancing the torque density. The authors in [21], [22], and [23] proposed different CP topologies, different winding configurations, and high PPN of PMs excitations into FR-PMM. It is found that the torque density can be greatly improved by utilizing toroidal winding and more pairs of PMs. Moreover, the authors in [24] and [25] extended the symmetric PMs excitation into asymmetric structure in order to fully generate the air-gap harmonics and further enhance the torque density. As for linear machine, Chung et al. [26] first proposed some types of CP structure for improving the force density while reducing the PMs usage. Kou et al. [27] put forward transverse-flux structure with different core types to achieve ultrahigh force density. The authors in [28], [29], [30], and [31] adopted asymmetric and hybrid excitation for FR-PMLM. In addition, Baker et al. [32] utilized more pairs of PMs to realize flux concentration and magnetic gearing effect in FR-PMLM. Zhao et al. [33] put forward Halbach arrays to enhance the force density while increasing the power factor. Even so, low-power factor and high-flux leakage issues in FR-PMLM still request more attention from the design and control aspects.

The main contribution of this article is the presentation of a novel series of asymmetric flux reversal permanent magnet linear machine (AFR-PMLM) that can achieve high-thrust force density due to their unique working mechanism. By adopting asymmetric PMs excitation, the AFR-PMLM effectively generates and fully utilizes the second-order harmonic magnetomotive force (MMF), leading to a notable improvement in thrust force density. In addition, the utilization of Halbach PMs array greatly improves the power factor.

The rest of this article is organized as follows. Section II introduces the machine topology and operational principles. In Section III, an improved MMF-permeance model that considers leakage flux is established to analytically calculate the air-gap flux density. The electromagnetic performances of the AFR-PMLM are comprehensively optimized and comparatively investigated in Sections IV and V, respectively. In Section VI, two prototypes of the AFR-PMLM are manufactured and tested

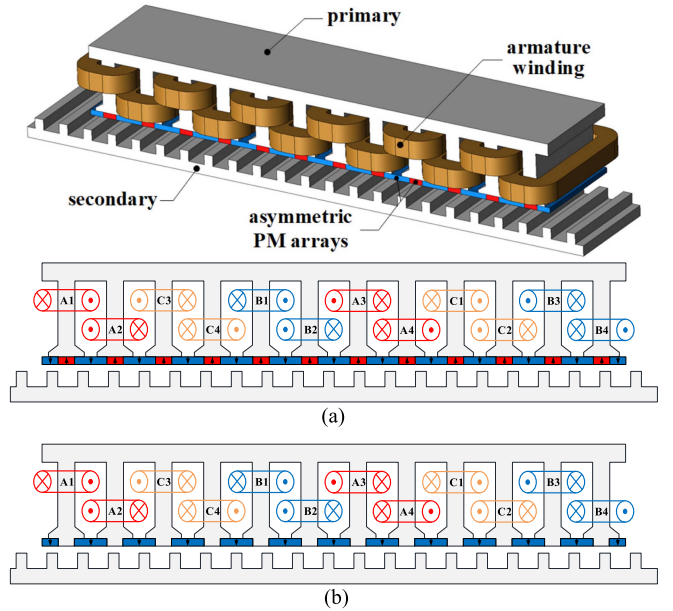


Fig. 1. Topologies of the proposed AFR-PMLM. (a) FP structure. (b) CP structure.

to validate the analysis results. Finally, Section VII concludes this article.

II. MACHINE TOPOLOGY AND OPERATION PRINCIPLE

Fig. 1 shows the topology of the proposed AFR-PMLM. The full pole (FP) structure shown in Fig. 1(a) contains two kinds of surface-mounted PMs with unequal width. When replacing the narrow kind of PMs with iron core, CP structure can be obtained in Fig. 1(b) with sole polarity. Moreover, double layer concentrated windings are inserted in the primary slots. The secondary is only made of salient iron core to modulate the MMF produced by the primary. In order to fully utilize the multi MMFs resulting from the asymmetric PMs excitation, the number of secondary poles (N_s) will be larger than that in near slot and pole combination existing in conventional PMLM.

Figs. 2 and 3 show the schematic of flux distribution under different positions and the corresponding open-circuit flux linkage, respectively. At position A (0°), where the first primary tooth aligns with the secondary tooth, the flux lines in Coil 1 move from the air gap to the back iron (marked as upward), while in Coil 2, the flux lines move from the back iron to the air-gap (marked as downward). Given that Coils 1 and 2 are connected in series but in opposite directions, this position results in a positive peak flux value, as illustrated in Fig. 3. Conversely, at position C (180°), where the second primary tooth aligns with the secondary tooth, the flux lines in both two coils flow in opposite directions compared with position A (0°), leading to a negative peak flux value. Furthermore, when the primary slot aligns with the secondary slot or tooth, as shown in Fig. 2(b) and (d), the PMs array only links the secondary and nearly no flux linkage can be obtained in the coils. Overall, as the secondary position varies within one pole pitch, the flux linkage in both two coils undergoes a 360 electrical

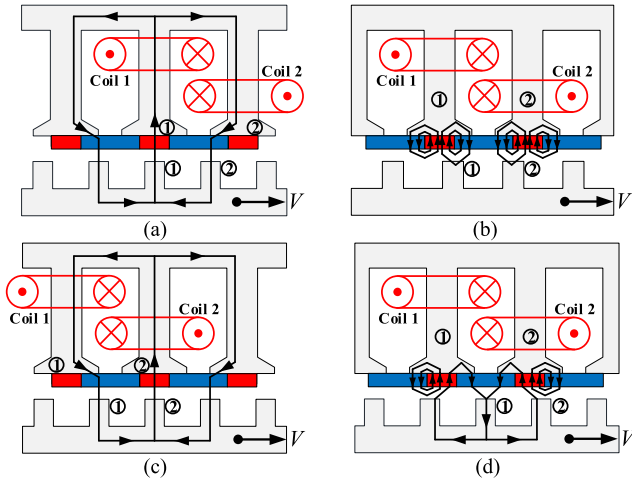


Fig. 2. Schematic of flux distribution at different positions. (a) Position A, 0°. (b) Position B, 90°. (c) Position C, 180°. (d) Position D, 270°.

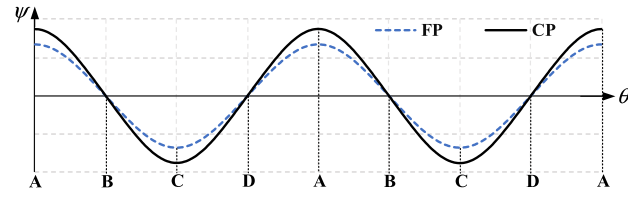


Fig. 3. Open-circuit flux linkage at different positions.

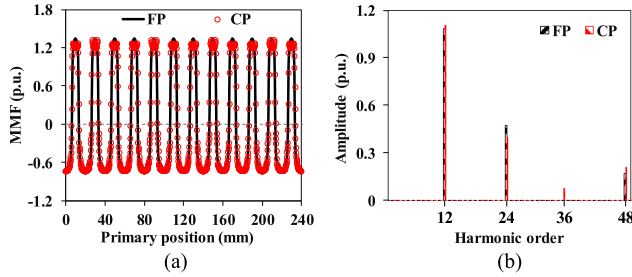


Fig. 4. MMF distribution of the proposed AFR-PMLM. (a) Waveforms. (b) Harmonics.

degree change, resulting in a sinusoidal and bipolar waveform. Moreover, since the surface-mounted PMs can be regarded as magnetic reluctance in the magnetic circuit, the flux linkage amplitude excited by the FP structure is smaller than that of CP structure.

Due to the asymmetric PMs excitation in both FP and CP structures, the waveform of MMF is also asymmetric and the positive and negative amplitudes are unequal, as shown in Fig. 4. Hence, even-order harmonic MMFs, such as second order and fourth order will appear as shown in Fig. 4(b) by using Fourier transform. It can be seen that the amplitude of second-order harmonic MMF nearly accounts for 40% of that in fundamental MMF, while the PMs volume is equal. Therefore, the MMFs in AFR-PMLM can be extended from odd-order distribution to integer-order distribution by using asymmetric PMs excitation. In order to fully utilize the even-order harmonic MMF especially the second-order harmonic MMF, the optimal slot-pole

TABLE I
FEASIBLE SLOT/POLE COMBINATIONS AND WINDING FACTOR

N_p	N_{pm}	N_s	7	8	10	11
6	6	k_p	0.5	0.866	0.866	0.5
		k_d	1	1	1	1
		k_w	0.5	0.866	0.866	0.5
9	9	N_s	11	13	14	16
		k_p	0.643	0.985	0.985	0.643
		k_d	0.960	0.960	0.960	0.960
12	12	k_w	0.617	0.946	0.946	0.617
		N_s	16	17	19	20
		k_p	0.866	0.966	0.966	0.866
15	15	k_d	1	0.966	0.966	1
		k_w	0.866	0.933	0.933	0.866
		N_s	20	22	23	25
18	18	k_p	0.866	0.995	0.995	0.866
		k_d	1	0.957	0.957	1
		k_w	0.866	0.952	0.952	0.866
21	21	N_s	25	26	28	29
		k_p	0.940	0.985	0.985	0.940
		k_d	0.960	0.960	0.960	0.960
24	24	k_w	0.902	0.946	0.946	0.902
		N_s	29	31	32	34
		k_p	0.931	0.997	0.997	0.931
27	27	k_d	0.956	0.956	0.956	0.956
		k_w	0.890	0.953	0.953	0.890
		N_s	34	35	37	38
30	30	k_p	0.966	0.991	0.991	0.966
		k_d	0.966	0.958	0.958	0.966
		k_w	0.933	0.949	0.949	0.933

combination in AFR-PMLM is different from the conventional PMLM with near slot-pole combination, which can be expressed as follows:

$$\begin{cases} N_p = 2mj, j = 1, 2, 3 \dots \\ N_s = 1.5N_p \pm k, k = 1, 2 \dots \end{cases} \quad (1)$$

where N_p is the number of primary slots, N_s is the number of secondary poles, and m is the phase number.

Based on (1), Table I presents several feasible slot/pole combinations that can be used for AFR-PMLM. The coil pitch factor (k_p), coil distribution factor (k_d) and winding factor (k_w) under different slot/pole combinations can be calculated as

$$\begin{cases} k_p = \sin(v\alpha/2) \\ k_d = \frac{\sin(bv\theta_s/2)}{b \sin(v\theta_s/2)} \\ k_w = k_p k_d \end{cases} \quad (2)$$

where α is the electrical degree between two conductors of a coil, b is the least number of different electromotive force (EMF) phasors for one phase, and θ_s is the electrical degree between two EMF phasors.

It can be deduced from Table I that the winding factor will also increase when the number of primary slots increases. The optimal slot/pole combination can be selected according to the actual force requirements and machine outer size. For example, when N_s is an even number, the force ripple in one electrical cycle is always larger than that when N_s is an odd number. Besides, since the amplitude of fundamental MMF is larger than second-order harmonic MMF, the flux linkage and induced back EMF will be larger when N_s is closer to the PPN of fundamental

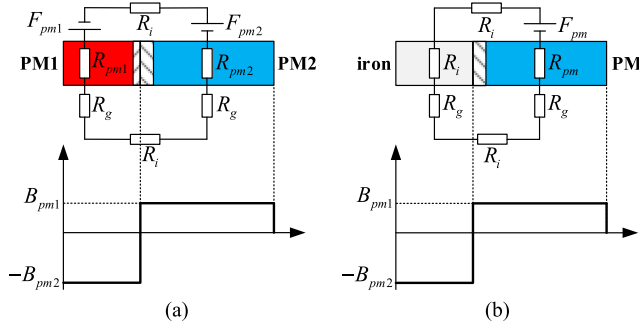


Fig. 5. Improved EMC models of asymmetric PMs excitation. (a) FP. (b) CP.

MMF. In this article, N_p is selected as 12, and then N_s can be 17/19 to achieve relatively high force density and low force ripple. For machines with other slots, similar selection also can be implemented.

III. ANALYTICAL MODELING AND CALCULATION

The proposed AFR-PMLM also obeys flux modulation theory and can be analytically calculated based on MMF-permeance model. To simplify the modeling and calculation, some assumptions are defined as follows.

- 1) The short primary is assumed to be static while the secondary translates with a velocity V .
- 2) The end effect, iron core reluctance, and magnetic saturation are neglected.
- 3) The primary slots are closed slots and the depth of secondary slots are regarded as infinite.

A. MMFs Produced By FP and CP

Fig. 5 shows the improved equivalent magnetic circuit (EMC) models of FP and CP structures in AFR-PMLM with a slotless secondary. The ideal air-gap flux density distribution can be calculated by using an improved EMC model, which considers the leakage flux at the internal edge of PMs excitation, and can be approximated as square waveforms. For the FP structure, the amplitude can be calculated as follows:

$$\begin{cases} B_{pm1} = 2(1-\gamma)B_r/(1+g\mu_r/h_m) \\ B_{pm2} = 2\gamma B_r/(1+g\mu_r/h_m) \\ \gamma \approx \alpha = w_{pml}/l_p \end{cases} \quad (3)$$

where g is the length of air gap, h_m is the PM height in the magnetized direction, α is the ratio of long PM width (w_{pml}) to slot pitch (l_p), and μ_r and B_r are the relative permeability and remanence of the PMs, respectively. Similarly, the amplitude of CP structure can be expressed as follows:

$$\begin{cases} B_{pm1} = B_r/(1+g\mu_r/[h_m(1-\gamma)]) \\ B_{pm2} = \frac{\gamma}{1-\gamma}B_{pm1} = \gamma B_r/(1-\gamma+g\mu_r/h_m) \\ \gamma = k_e/(k_e-1+1/\alpha), k_e \approx (w_{pml}-3)/w_{pml} \end{cases} \quad (4)$$

where k_e is the coefficient representing the ratio of effective length of long PM that contributes to main flux to the actual length. The coefficient k_e is essential for correcting the amplitude of the MMF, primarily due to the influence of leakage flux in

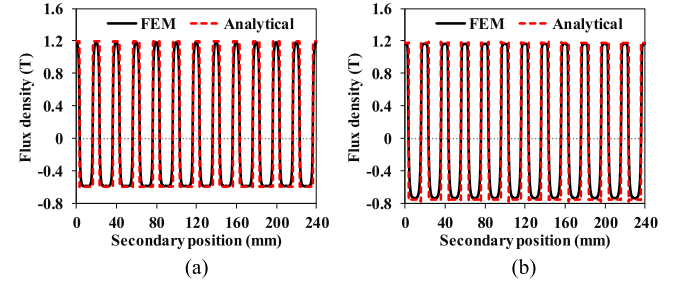


Fig. 6. Air-gap flux density distribution of AFR-PMLM with a slotless secondary. (a) FP. (b) CP.

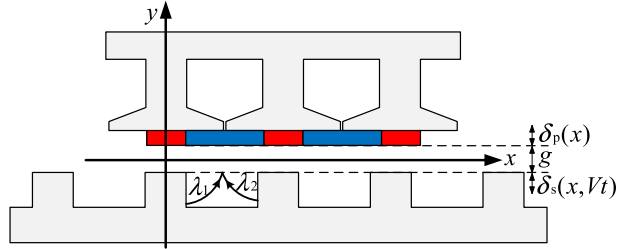


Fig. 7. Schematic of salient structure and air-gap permeance.

the internal edge of the CP structure. Then, the ideal air-gap flux density without accounting for the secondary slot is defined as B_{pm} and can be calculated as

$$B_{pm}(x) = \sum_{i=1}^{\infty} \frac{-2 \sin [(1-\gamma)i\pi]}{i\pi} B_{pm1} \cos \left[iN_{pm} \frac{2\pi}{N_p l_p} x \right] \quad (5)$$

where the amplitude B_{pm1} is different for FP and CP structures. On this basis, the MMF produced by FP and CP structures can be expressed as

$$\begin{cases} F_{pm}(x) = g_e B_{pm}/\mu_0 \\ g_e = g + \delta_p(x) \end{cases} \quad (6)$$

where g_e is the effective length of air gap, which includes an additional air gap $\delta_p(x)$ caused by the PMs in FP structure and the primary slots in CP structure. In addition, the MMF can be represented using a Fourier series as follows:

$$F_{pm}(x) = \sum_{i=1}^{\infty} \frac{-2 \sin [(1-\gamma)i\pi]}{i\pi} \frac{B_{pm1}}{\mu_0/g_e} \cos \left[iN_{pm} \frac{2\pi}{N_p l_p} x \right]. \quad (7)$$

Fig. 6 presents the air-gap flux density distribution of AFR-PMLM with a slotless secondary. It indicates that the analytical results for both FP and CP agree well with the FEM counterpart, which can effectively validate the accuracies of the improved MMF modeling in (3)–(7). Moreover, it is clear that the PPN of PMs is 12 and the positive and negative parts of the waveforms are asymmetric due to the unequal widths of PMs.

B. Air-Gap Permeance

Fig. 7 shows the schematic of salient structure and air-gap permeance. Due to the large slotting structure in the secondary,

additional air gap $\delta_s(x)$ is utilized to represent the equivalent air gap in the secondary. By assuming that the flux line is quarter circular, the length of flux λ_1 and λ_2 can be calculated as

$$\begin{cases} \lambda_1 = \pi (x - w_{st}/2) / 2 \\ \lambda_2 = \pi (\tau_p - w_{st}/2 - x) / 2. \end{cases} \quad (8)$$

Then, additional air gap $\delta_s(x)$ in one pole pitch can be regarded as a parallel connection of the flux λ_1 and λ_2 , which can be expressed as

$$\begin{aligned} \delta_s(x, t) &= \\ &= \begin{cases} 0, x \notin [Vt + w_{st}/2, Vt + \tau_p - w_{st}/2] \\ \lambda_1 \lambda_2 / (\lambda_1 + \lambda_2), x \in [Vt + w_{st}/2, Vt + \tau_p - w_{st}/2] \end{cases} \end{aligned} \quad (9)$$

where w_{st} is the width of secondary tooth. Then, the air-gap permeance Λ can be expressed as (10) based on the primary permeance (Λ_p) and secondary permeance (Λ_s), respectively. It should be noted that these permeances also can be expressed as Fourier series forms

$$\begin{cases} \Lambda_p(x, t) = \mu_0 / (g + \delta_p(x, t)) \\ \Lambda_s(x, t) = \mu_0 / (g + \delta_s(x, t)) \\ \Lambda(x, t) = \mu_0 / (g + \delta_p(x) + \delta_s(x, t)) \approx g\Lambda_p\Lambda_s/\mu_0. \end{cases} \quad (10)$$

C. Flux Density Distribution

When multiplying the MMF in (7) by the air-gap permeance in (10), the air-gap flux density of AFR-PMLM with a slotted secondary can be calculated as

$$B_g(x, t) = F_{pm}(x) \Lambda(x, t) = B_{pm}(x) \Lambda_{rel} = B_{pm}(x) \frac{g\Lambda_s}{\mu_0} \quad (11)$$

where Λ_{rel} is the relative air-gap permeance and equals to $g\Lambda_s/\mu_0$. It means that the calculation of air-gap flux density can be simplified to the multiplication of B_{pm} in (5) with Λ_{rel} that is only related to the secondary permeance (Λ_s). By expressing the secondary permeance in Fourier series forms, the air-gap flux density also can be written as

$$\begin{aligned} B_g(x, t) &= \sum_{i=1,2,3}^{\infty} \Lambda_{s0} B_{ci} \cos \left[iN_{pm} \frac{2\pi}{N_p l_p} x \right] \\ &+ \frac{1}{2} \sum_{k=1,3,5}^{\infty} \sum_{i=1,2,3}^{\infty} \Lambda_{sk} B_{ci} \cos \left[(iN_{pm} - kN_s) \right. \\ &\times \left. \frac{2\pi}{N_p l_p} \left(x + \frac{kN_s}{iN_{pm} - kN_s} Vt \right) \right] \\ &+ \frac{1}{2} \sum_{k=1,3,5}^{\infty} \sum_{i=1,2,3}^{\infty} \Lambda_{sk} B_{ci} \cos \left[(iN_{pm} + kN_s) \right. \\ &\times \left. \frac{2\pi}{N_p l_p} \left(x - \frac{kN_s}{iN_{pm} + kN_s} Vt \right) \right] \end{aligned} \quad (12)$$

$$B_{ci} = -\frac{g}{\mu_0} \frac{2}{i\pi} \frac{\sin[(1-\gamma)i\pi]}{1-\gamma} B_{pm1} \quad (13)$$

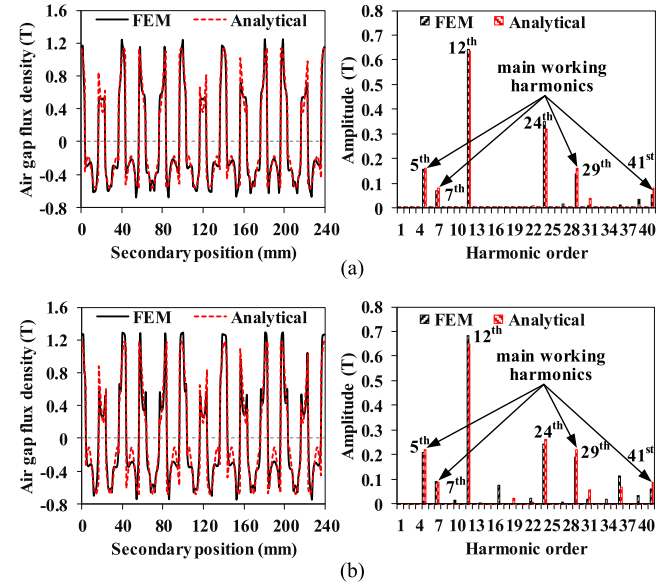


Fig. 8. Air-gap flux density distribution and harmonics of AFR-PMLM with slotted secondary. (a) FP. (b) CP.

TABLE II
HARMONICS ANALYSIS OF AIR-GAP FLUX DENSITY

	PPN	Speed (Mech.)	Speed (Elec.)
Stationary	iN_{pm}	0	0
Moving	$iN_{pm} + kN_s$	$2\pi kN_s / (iN_{pm} + kN_s) / N_p l_p$	$2\pi kN_s V / N_p l_p$
	$iN_{pm} - kN_s > 0$	$-2\pi kN_s / (iN_{pm} - kN_s) / N_p l_p$	$-2\pi kN_s V / N_p l_p$
	$iN_{pm} - kN_s < 0$	$-2\pi kN_s / (iN_{pm} - kN_s) / N_p l_p$	$2\pi kN_s V / N_p l_p$

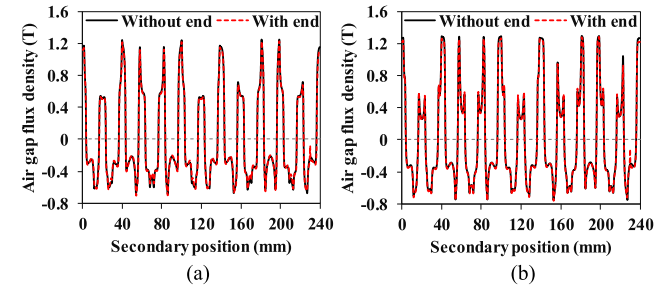


Fig. 9. Air-gap flux density distribution with/without considering the end effect. (a) FP. (b) CP.

where Λ_{s0} and Λ_{sk} are the zero order and k th harmonic amplitudes of secondary permeance, respectively.

Fig. 8 shows the air-gap flux density distribution and harmonics of AFR-PMLM with a slotted secondary. The predicted analytical results agree well with the FEM results. The harmonics of air-gap flux density in terms of PPN and speed can be concluded in Table II. The harmonics with the PPN of iN_{pm} (12th and, 24th) are stationary, while the harmonics with the PPN of $|iN_{pm} \pm kN_s|$ (fifth, seventh, 29th, and 41st) are moving and can induce back EMF in the winding. It should be noted that when $iN_{pm} - kN_s > 0$, these harmonics are moving in the opposite direction and the speed is marked as negative value. In addition, these harmonics also can be regarded as contributing negative amplitude from the perspective of back EMF. Fig. 9 presents the air-gap flux density

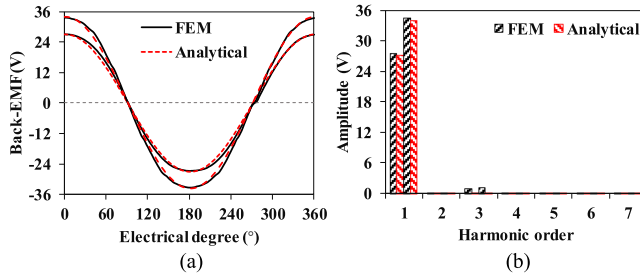


Fig. 10. Comparison of phase back EMFs and harmonics of AFR-PMLM. (a) Waveforms. (b) Harmonics.

distribution with and without considering the end effect. The results indicate that the waveforms of flux density under these two conditions are highly similar, suggesting that the end effect has a negligible impact. Thus, the assumption of neglecting the end effect is rational, and it does not significantly affect the distribution of the working harmonics.

D. Flux Linkage, Back EMF, and Thrust Force

After obtaining the air-gap flux density, the flux linkage can be calculated as

$$\psi_A(t) = l_{\text{stk}} \int_0^{N_p l_p} B_g(x, t) N_A(x) dx \quad (14)$$

where l_{stk} is the stack length of the machine, $N_A(x)$ is the winding function, and can be calculated as follows:

$$N_A(x) = \sum_{j=1,3,5}^{\infty} \frac{2}{j P_a \pi} N_c k_{wj} \cos \left(j P_a \frac{2\pi}{N_p l_p} x \right) \quad (15)$$

where N_c is the series connected winding turns per phase, k_{wj} is the winding factor of the j th air-gap flux density. It can be deduced that only when the PPN of armature winding $P_a = |iN_{\text{pm}} \pm kN_s|$, time-varied flux linkage can be produced in the armature winding. Hence, the phase back EMF can be calculated as

$$\begin{aligned} E_A(t) &= -\frac{d\psi_A}{dt} = -\frac{d \left(l_{\text{stk}} \int_0^{N_p l_p} B_g(x, t) N_A(x) dx \right)}{dt} \\ &= \sum_{k=1,3,5}^{\infty} \sum_{i=1,2,3}^{\infty} 2l_{\text{stk}} B_{ki} N_c k N_s V \left(\frac{k_{wa}}{a} - \frac{k_{wb}}{b} \right) \\ &\quad \times \sin \left(k N_s \frac{2\pi}{N_p l_p} Vt \right) \\ a &= iN_{\text{pm}} + kN_s, b = iN_{\text{pm}} - kN_s, B_{ki} = \frac{1}{2} \Lambda_{sk} B_{ci}. \end{aligned} \quad (16)$$

Fig. 10 presents the comparison of phase back EMFs and harmonics of AFR-PMLM based on (16). The analytical results agree well with the FEM predicted results, where the fundamental amplitude of CP is about 20% higher than that of FP. When only considering the fundamental waveform of the back EMF (i.e., $k = 1$) and injecting sinusoidal current with the amplitude

TABLE III
HARMONIC AMPLITUDES AND FORCE CONTRIBUTIONS OF AFR-PMLM

Items	FP	CP
$ N_{\text{pm}} \pm N_s 5^{\text{th}}, 29^{\text{th}}$	Amplitude (T)	0.167
	Force (N)	189.5
$ 2N_{\text{pm}} \pm N_s 7^{\text{th}}, 41^{\text{st}}$	Amplitude (T)	0.083
	Force (N)	67.5
$ 3N_{\text{pm}} \pm N_s 19^{\text{th}}, 53^{\text{rd}}$	Amplitude (T)	6.0e-4
	Force (N)	0.1
		11.1

of I_m , the electromagnetic force can be calculated as

$$F_{\text{avg}} = \sum_{i=1,2,3}^{\infty} 3l_{\text{stk}} B_{ki} N_c N_s V I_m \left(\frac{k_{wa}}{a} + \frac{k_{wb}}{|b|} \right) \quad (17)$$

where a and b are equal to those in (16). In addition, it is worth noting that the sign for b differs between (16) and (17) since the harmonics with the PPN of b make varying contribution in back EMF and thrust force, respectively. As mentioned in Table II, when $iN_{\text{pm}} - kN_s > 0$, the harmonics with the PPN of b are moving in the opposite direction as other harmonics. Hence, these harmonics can be regarded as contributing negative amplitude of back EMF. However, because the winding phase sequence used for these oppositely moving harmonics with the PPN of b is also reversed, the air gap contains the oppositely moving harmonics and the reverse armature field, resulting in a positive thrust force. Table III lists the harmonic amplitude and force contribution of AFR-PMLM. It shows that the fundamental MMF contributes nearly 75% of the average force while the second-order MMF contributes more than 20% of the average force. It should be noted that this analytical result may be smaller than the FEM result since only fundamental permeance ($k = 1$) is calculated.

IV. DESIGN AND GLOBAL OPTIMIZATION

In order to maximize the thrust force of AFR-PMLM under specific volume, both FP and CP structures are globally optimized by using multi-objective genetic algorithm coupled with FEM under the identical machine outer sizes: i.e., machine length is 240 mm, machine height is 45 mm, stack length (l_{stk}) is 50 mm, and air gap is 0.8 mm. Moreover, the PMs are N48UH and the lamination materials are 50DW470. The objective function for optimization can be expressed as follows:

$$\begin{aligned} \min F(\mathbf{x}) &= [f_j(\mathbf{x})]^T, \mathbf{x} = [x_i]^T \\ \text{s.t. } x_i &> 0 \end{aligned} \quad (18)$$

where x_i are the geometric parameters that need to be optimized and have been marked in Fig. 11, $f_j(\mathbf{x})$ are two objective functions, i.e., the negative thrust force and the force ripple, which can maximize the average force and minimize the force ripple. Genetic algorithm (GA) is capable of finding the optimal design through natural selection, which involves three operators: selection, crossover, and mutation. The geometric parameters are coded, and each solution is represented by a chromosome. The number of populations and generations in GA is selected as 50 and 50, respectively. Moreover, the crossover and mutator

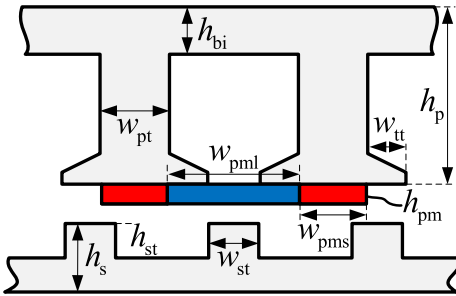


Fig. 11. Geometric parameters of AFR-PMLM.

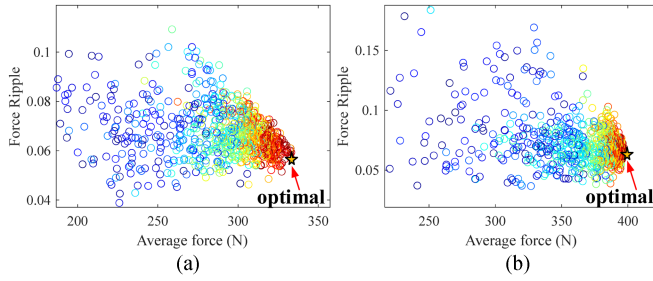


Fig. 12. Optimization results of 12s17p AFR-PMLM. (a) FP. (b) CP.

TABLE IV
DESIGN PARAMETERS OF 12S17P AFR-PMLM

Symbol	Parameters	Units	FP	CP
Globally optimized geometric parameters				
τ	Secondary pole pitch	mm	14.12	
k_{sr}	Split ratio	/	0.25	
w_{pt}	Primary tooth width	mm	7.0	
w_{pms}	Small PM/Iron width	mm	6.7	
w_{pml}	Large PM width	mm	13.3	
h_{pm}	PM height	mm	1.5	2.5
w_{tt}	Tooth tip width	mm	3.5	
h_p	Primary height	mm	33.7	
h_{bi}	Back iron height	mm	6.0	
h_{st}	Secondary pole height	mm	5.0	
w_{st}	Secondary pole width	mm	4.9	
h_s	Secondary height	mm	10.2	
Rated data				
k_f	Copper filling factor	/	0.55	
P_{cop}	Rated copper loss	W	200	
N	Number of turns	/	118	113
I	Rated phase current	A	6.2	6.4

factors are 0.9 and 0.1, respectively. Fig. 12 shows the optimization results of 12s17p AFR-PMLM for both FP and CP structures. With the evolution of GA, the cases will converge from blue circles to an optimal region with red circles. Finally, the optimal case is selected from these red circles, of which the optimal design parameters are listed in Table IV.

This section also makes sensitivity analysis for assessing the impact of geometric parameters on objectives. The sensitivity S_i can be calculated as

$$S_i = \frac{V [E(f|x_i)]}{V(f)} \quad (19)$$

where f represents the objective function, $E(f|x_i)$ represents the expected value when parameter x_i is fixed, and V is the variance.

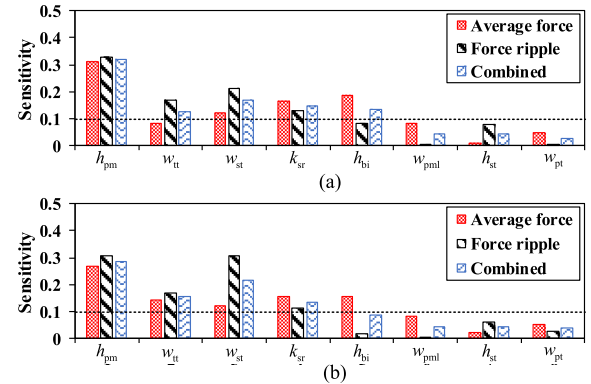


Fig. 13. Sensitivity analysis of geometric parameters. (a) FP. (b) CP.

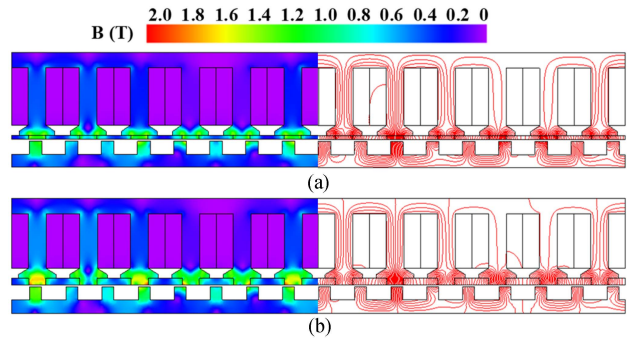


Fig. 14. Open-circuit magnetic field distribution of 12s17p AFR-PMLM. (a) FP. (b) CP.

TABLE V
FORCE PERFORMANCE UNDER DIFFERENT SLOT/POLE COMBINATIONS

	6s8p	6s10p	9s13p	9s14p	12s17p	12s19p
FP	263.6 N (91.0%)	300.2 N (33.8%)	338.3 N (12.2%)	341.3 N (11.8%)	332.5 N (4.7%)	327.3 N (4.5%)
CP	288.4 N (81.5%)	327.2 N (34.3%)	391.1 N (13.2%)	390.7 N (15.8%)	396.3 N (6.2%)	373.4 N (7.5%)
	15s22p	15s23p	18s26p	18s28p	21s31p	21s32p
FP	295.9 N (5.6%)	288.8 N (5.0%)	257.1 N (7.7%)	238.8 N (7.9%)	206.2 N (8.2%)	198.3 N (9.9%)
CP	341.7 N (5.8%)	332.0 N (7.9%)	296.8 N (9.6%)	275.2 N (11.9%)	242.2 N (9.8%)	234.0 N (11.6%)

Fig. 13 provides the sensitivity analysis of different geometric parameters, which can be categorized into two groups: sensitive parameters ($S_i \geq 0.1$) and insensitive parameters ($S_i < 0.1$). The combined sensitivity takes both the influence on average force and force ripple into consideration. It is apparent that the PM height, tooth tip width, secondary pole width, and split ratio have a significant impact on both the average force and force ripple. Therefore, it is crucial to pay attention to these sensitive parameters during the practical manufacturing process.

Table V provides a comparative study of the average force and force ripple for different slot/pole combinations. All configurations have the same outer dimensions and undergo global optimization. It is observed that the average forces are relatively higher when the primary slots are set to 9 and 12. In addition, the force ripples are relatively lower when the primary slots are set to

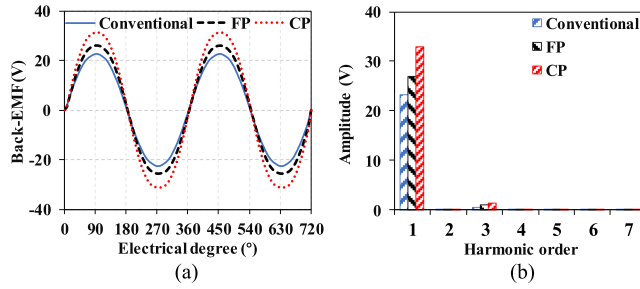


Fig. 15. Open-circuit phase back EMF of AFR-PMLM at $v = 1.0$ m/s.
(a) Waveforms. (b) Harmonics.

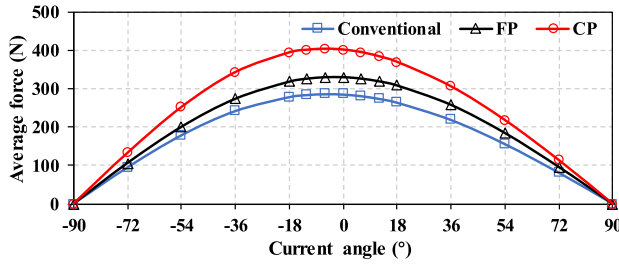


Fig. 16. Variation of average force with different current angles.

12 and 15. Based on these findings, the most optimal slot/pole combination for the specified outer dimensions appears to be 12s17p.

V. ELECTROMAGNETIC PERFORMANCE ANALYSIS

A. Open-circuit Characteristics

The electromagnetic performances of the optimal design are deeply evaluated by the finite element method. Fig. 14 provides the open-circuit magnetic field distribution of 12s17p AFR-PMLM. As can be seen, the primary tooth near the PMs excitation is more saturated due to the inevitable leakage flux of the FR structure, while the middle of the primary tooth and the back iron is less saturated. Moreover, CP structure is more saturated than FP structure since the equivalent air-gap length is small. Fig. 15 presents the open-circuit phase back EMF of AFR-PMLM at a velocity of $v = 1.0$ m/s. To illustrate the advantages of asymmetric excitation more intuitively, a conventional 12s13p FR-PMLM with symmetric excitation is set as a benchmark. All three types of machines exhibit sinusoidal back EMF with very low third-order harmonic. It is evident that the fundamental amplitude of FP and CP structures is 15.9% and 44.3% higher compared with the conventional structure, respectively.

B. Thrust Force Performances

Fig. 16 presents the variation of average force with different current angles. It is observed that the maximum average force can be achieved when the current angle is between 0 to -6. This indicates that the proposed AFR-PMLM operates similarly to the conventional FR-PMLM, which does not generate reluctance force. As a result, the commonly used $i_d = 0$ control strategy can be fully utilized. In addition, FP and CP structures can provide

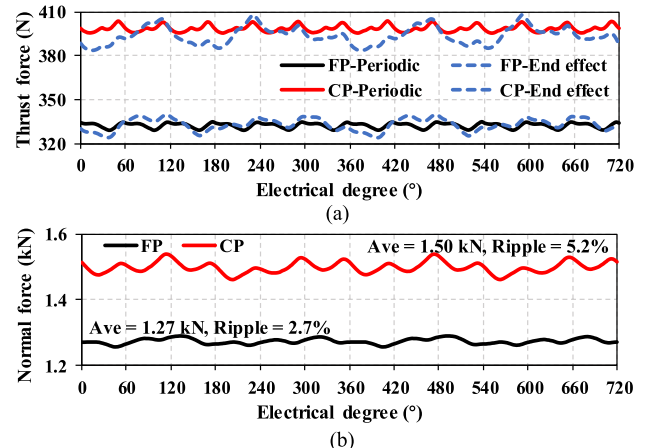


Fig. 17. Waveform of force distribution under rated condition.
(a) Thrust force. (b) Normal force.

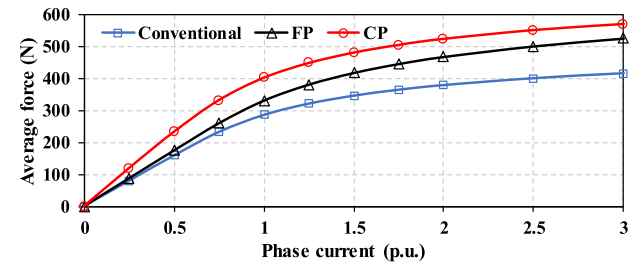


Fig. 18. Variation of average force with different phase currents.

15.0% and 40.1% higher average force than conventional FR-PMLM under rated condition.

Fig. 17 shows the waveform of force distribution under rated condition, including the thrust force in 17(a) and normal force in 17(b). The longitudinal end effect in linear machines inevitably adds end force into the thrust force, causing a certain degree of increase in thrust force ripple. Specifically, for FP and CP structures, the thrust force ripple increases from 2.0% to 4.7% and 6.2%, respectively. In addition, Fig. 17(b) presents the normal force distribution of the proposed AFR-PMLM. The results indicate that the normal force for FP and CP structures is approximately 1270 and 1500 N, respectively. This is about 3.8 times of the rated thrust force for both structures. This normal force can be effectively used as levitation force when AFR-PMLM is used in a Maglev system. The normal force in AFR-PMLM is much smaller than that in conventional PMLM. However, in certain PE-PMLM, such as SF-PMLM, the normal force may surpass that of conventional PMLM. Therefore, it is essential to give special attention to assembly issues.

Fig. 18 further investigates the variation of average force with phase currents under $i_d = 0$ control strategy. Due to the inevitable leakage flux and saturation in the primary tooth, the overload capability of the proposed AFR-PMLM is weak. When the phase current is increased to two times of the rated value, the average force can only achieve 1.41 and 1.30 times of the rated value for FP and CP structures, respectively. Even when the phase current is increased to three times of the rated value, no more than 1.6

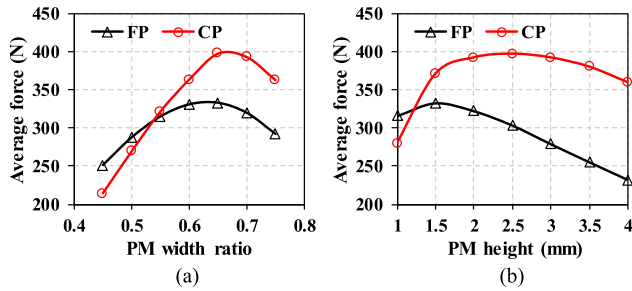


Fig. 19. Variation of average force with PM geometric sizes. (a) PM width ratio. (b) PM height.

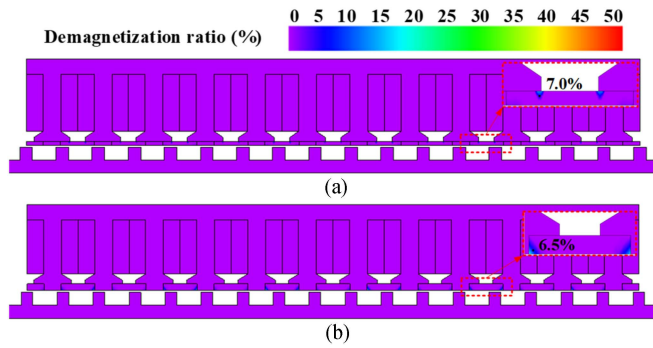


Fig. 20. Demagnetization ratio under three times of rated current and 100 °C. (a) FP. (b) CP.

times of the rated force can be achieved. Since the MMF and thrust force is highly related to the geometric sizes of asymmetric PM array, this article presents the variation of average force with PM geometric sizes in Fig. 19. The PM width ratio is defined as the ratio of long PM to slot pitch. It clearly shows that when the PM width ratio is about 2/3, AFR-PMLM can maximize the use of multiple harmonics and obtain the maximum average force. FP structure requires less PM height to realize the maximum average force in order to reduce the equivalent air-gap length for armature field.

C. Demagnetization Risk

To explore the irreversible demagnetization risk of the PMs in FP and CP structures, this article utilizes demagnetization ratio (k_{dem}) to measure the demagnetization level as: $k_{\text{dem}} = 1 - B_d / B_i$, where B_i the initial remanence and B_d is the remanence after demagnetization. To assess the demagnetization situation, a negative d -axis current with three times of the rated value is applied at a working temperature of 100 °C. Fig. 20 plots the demagnetization ratio distribution in different areas of FP and CP structures. The results indicate that demagnetization within a 10% ratio only occurs in a small area near the corner of the tooth and tooth tip. However, the majority of the area does not exhibit any risk of demagnetization.

In addition, this article examines the impact of demagnetization on back EMF by utilizing the results obtained from irreversible demagnetization of the PMs. Table VI presents the fundamental amplitude of back EMF after demagnetization at various negative d -axis currents and a temperature of 100 °C. The findings indicate that the FP structure carries a higher risk

TABLE VI
FUNDAMENTAL AMPLITUDE OF BACK EMF AFTER DEMAGNETIZATION

Negative d -axis current (p.u.)	FP		CP	
	Amp. (V)	Diff.	Amp. (V)	Diff.
Original	26.7	/	35.6	/
5.0	25.5	-4.5%	35.2	-1.1%
10.0	23.5	-12.0%	34.8	-2.2%

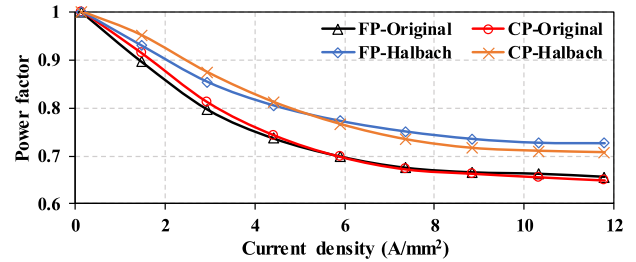


Fig. 21. Variation of power factor with different current densities.

of demagnetization compared with the CP structure, primarily due to its series excitation type and shorter PM height. However, this risk can be mitigated by increasing the PM height. On the other hand, the CP structure demonstrates minimal risk of demagnetization even when subjected to ten times of rated negative d -axis current.

D. Power Factor Analysis

Due to the inevitable leakage flux in PM array, FR-PMLM has an inherent weakness of low power factor. The power factor in AFR-PMLM can be simplified and expressed as

$$\text{PF} = \cos \varphi \approx 1 / \sqrt{1 + \left(\frac{\omega_e L_s I}{E_0} \right)} \quad (20)$$

where ω_e is the angular velocity, L_s is synchronous inductance, and E_0 is the induced back EMF.

Fig. 21 presents a comparison of the power factor between employing the Halbach PMs array and the original PMs excitation. The findings indicate that the Halbach PMs array can effectively enhance the power factor by minimizing the leakage flux. Even at high current densities exceeding 10 A/mm², the power factor can be enhanced to surpass 0.7. More importantly, the utilization of the Halbach PMs array allows for simultaneous improvement in the thrust force density. Although the power factor may decrease under high current density, the average power factor in the AFR-PMLM remains acceptable considering the short-time duty cycle for linear motion. Moreover, when designing the inverter capacity, the power factor under peak current density should be taken into consideration.

E. Electromagnetic Performance Comparison

In order to evaluate the electromagnetic performance of the proposed AFR-PMLM, this section conducts a fair comparison with conventional SF-PMLM and PMLM of identical external dimensions and a copper loss of 200 W. Both of these two machines have undergone global optimization, and their

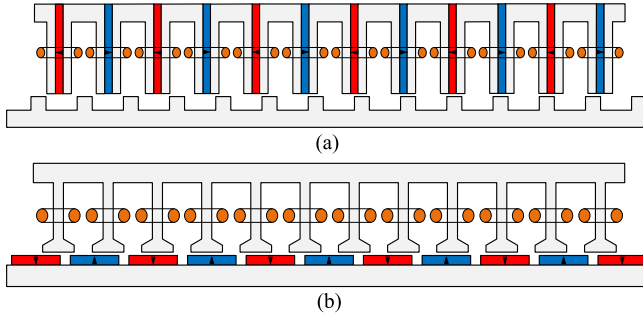


Fig. 22. Topologies of benchmark machines. (a) Conventional SF-PMLM. (b) Conventional PMLM.

TABLE VII
RATED PERFORMANCE COMPARISON BETWEEN SEVERAL PMLMs

Performance	Conv. SF-PMLM	Conv. PMLM	Proposed AFR-PMLM	
			FP	CP
Average force (N)	438.2	528.3	332.5	396.3
Detent force (N)	23.0	56.4	8.4	15.1
Force ripple (%)	10.9	16.3	4.7	6.2
PM Vol. (mL) (@10 m)	50.6	1660.0	18.0	20.0
Force density (N/cm ²)	3.65	4.40	2.77	3.30
Force/Copper loss (N/W)	2.19	2.64	1.66	1.98
Power factor	0.88	0.94	0.67	0.67

topologies are depicted in Fig. 22. The main distinction between the conventional PMLM and the novel PE-PMLMs lies in the placement of PMs, as conventional PMLM requires the entire range of the secondary for mounting.

Table VII provides a performance comparison of the four PMLMs at their rated conditions ($P_{\text{cop}} = 200$ W). Compared with SF-PMLM, the proposed AFR-PMLM with CP structure only consumes nearly 39.5% of the PMs volume while providing about 90.4% of the thrust force. More importantly, the structure and assembly of AFR-PMLM is much simpler than SF-PMLM. In addition, the thrust force density of AFR-PMLM is about 75.0% of conventional PMLM. Due to the necessity of surface mounting PMs across the entire length of the long stator, the PMs consumption in conventional PMLM exceeds that in the AFR-PMLM by more than 80 times for a long distance of 10 m. Furthermore, Table VII includes the calculation of the force-to-copper loss index, in which a larger value indicates a larger thrust force for the same copper loss. Regarding the power factor, the proposed AFR-PMLM achieves nearly 70% of the power factor of the conventional PMLM, which is about 24% lower than that of SF-PMLM. However, by adopting the Halbach PM array, the proposed AFR-PMLM can provide a power factor similar to that of SF-PMLM. Overall, it can be concluded that AFR-PMLM is a competitive candidate for low-cost long excursion application compared with conventional PMLM as well as the existing PE-PMLMs.

VI. EXPERIMENTAL VALIDATION

In order to validate the electromagnetic performances of AFR-PMLM that investigated by FEM, two prototypes of 12s17p

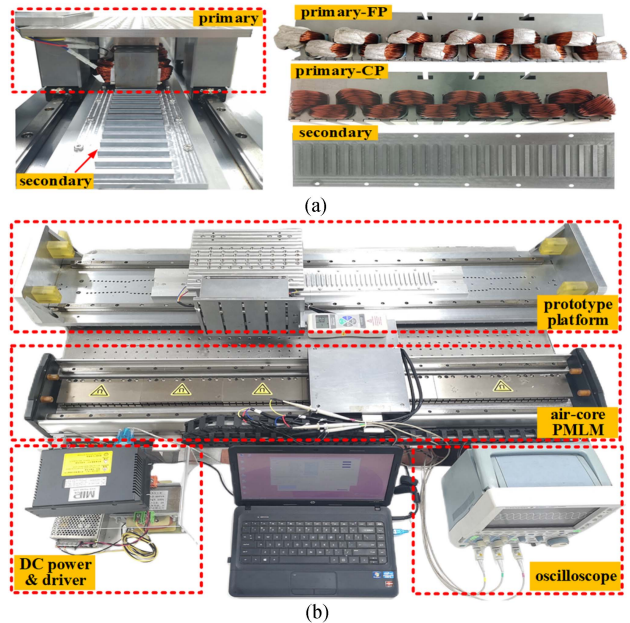


Fig. 23. Prototype and test bench for experiment. (a) Prototype of 12s17p AFR-PMLM. (b) Test bench.

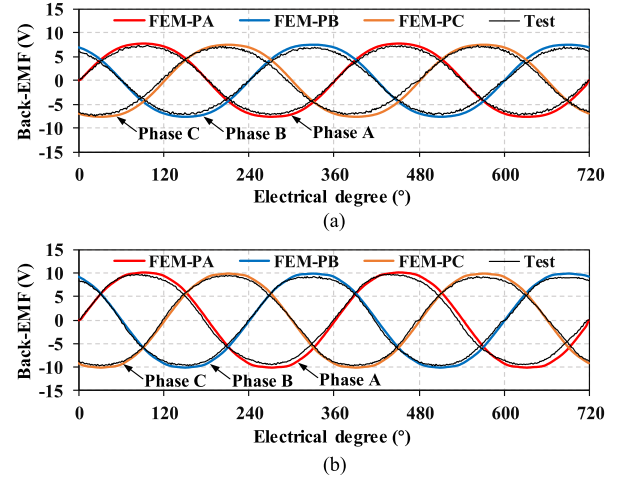


Fig. 24. Test results of three phases open-circuit back EMFs when $v = 0.3$ m/s. (a) FP. (b) CP.

AFR-PMLM with FP and CP structures are designed and manufactured in this section. Fig. 23(a) shows the FP and CP prototypes for experiment, where the machine sizes are the same as those in Table II. The primary is assembled on a mover that leaded by two linear guides, and the secondary is assembled on the stator between two linear guides. Fig. 23(b) shows the experimental test bench that contains two parts, i.e., one prototype platform and one air-core PMLM. In addition, these two parts are connected through a force meter, which can record the real-time acting force.

Fig. 24 presents the test results of three phases open-circuit back EMFs for both FP and CP structures. The air-core PMLM is driven by an inverter to provide 0.3 m/s steady-state motion for the prototype. It can be seen that the test results for both

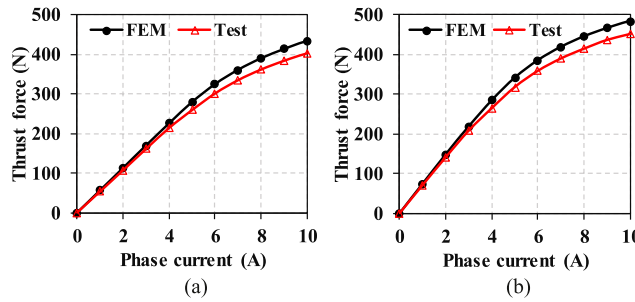


Fig. 25. Test results of thrust force with phase currents. (a) FP. (b) CP.

TABLE VIII
TEST RESULTS OF POWER FACTOR AT 0.3 M/S

Current density (A/mm ²)	FP			CP		
	FEM	Test	Error	FEM	Test	Error
1.0	0.94	0.92	2.1%	0.95	0.92	3.2%
3.0	0.79	0.75	5.1%	0.80	0.75	6.3%
5.0	0.72	0.67	6.9%	0.72	0.67	6.9%
7.0	0.68	0.63	7.4%	0.67	0.63	6.0%
10.0	0.66	0.61	7.6%	0.66	0.61	7.6%

FP and CP structures are close to the FEM counterparts, where the three phase discrepancies are within 7.9%, 9.5%, and 9.2% for FP structure and are within 6.5%, 7.0%, and 6.8% for CP structure, respectively. In addition, the unbalance between three phase windings is within 1.5% and can be neglected.

Fig. 25 presents the test results of thrust force with different phase currents. It shows that the variation of tested thrust force results is consistent with the FEM predicted results for both FP and CP structures. With the increase of phase current, the prototype will be more saturated and the discrepancies between the FEM and test results will also increase, where the maximum discrepancies under high phase current are within 7.2% and 7.8%, respectively. In addition, Table VIII provides the test results of power factor under different current densities. The machine operates at 0.3 m/s steady-state velocity. As the current density increases, the power factor gradually decreases. The tested power factors are slightly smaller than the predicted results due to the practical influence of loss and temperature. Overall, it can be concluded that the FEM predicted results agree well with the experimental results, and the proposed AFR-PMLM can achieve the design index.

VII. CONCLUSION

This article investigates two kinds of AFR-PMLM with asymmetric excitation for low-cost long excursion application. The thrust force generation mechanism under multi MMFs is analytically calculated based on the flux modulation theory. The proposed AFR-PMLM is globally optimized and the electromagnetic performances are comprehensively researched. Some conclusions can be drawn as follows.

- With the help of asymmetric excitation, second-order harmonic MMF also can be effectively utilized to generate the thrust force, which contributes more than 20% of the total thrust force. The utilization of multi MMFs and multi

harmonics is an effective approach to enhance the thrust force density.

- In terms of thrust force, the proposed AFR-PMLM with FP and CP structures can provide 15.0% and 40.1% higher average force than conventional FR-PMLM under rated condition. Besides, CP structure only consumes nearly 39.5% of the PMs volume while providing about 90.4% of the thrust force compared with SF-PMLM. More importantly, the structure and assembly of AFR-PMLM is much simpler than SF-PMLM.
- For a long excursion with 10 m, AFR-PMLM consumes only 1/80 PMs volume while can achieve 75.0% of the thrust force density compared with conventional PMLM. Therefore, AFR-PMLM is a competitive candidate for low cost long excursion application compared with conventional PMLM as well as the existing PE-PMLMs.

REFERENCES

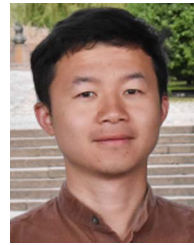
- I. Boldea, L. N. Tutelea, W. Xu, and M. Pucci, "Linear electric machines, drives, and MAGLEVs: An overview," *IEEE Trans. Ind. Electron.*, vol. 65, no. 9, pp. 7504–7515, Sep. 2018.
- Q. Lu, Y. Shen, and Y. Ye, "Development of permanent magnet linear synchronous motors structure and research," *Proc. CSEE*, vol. 39, no. 9, pp. 2575–2587, May 2019.
- C. Guo et al., "Review of recent advances of free-piston internal combustion engine linear generator," *Appl. Energy*, vol. 269, Jul. 2020, Art. no. 115084.
- X. Huang, J. Liang, B. Zhou, C. Zhang, L. Li, and D. Gerada, "Suppressing the thrust ripple of the consequent-pole permanent magnet linear synchronous motor by two-step design," *IEEE Access*, vol. 6, pp. 32935–32944, 2018.
- X. Xu, Z. Sun, B. Du, and L. Ai, "Pole optimization and thrust ripple suppression of new Halbach consequent-Pole PMLSM for ropeless elevator propulsion," *IEEE Access*, vol. 8, pp. 62042–62052, 2020.
- Y. Zhou, R. Qu, Y. Gao, C. Shi, and C. Wang, "Modeling and analyzing a novel dual-flux-modulation consequent-pole linear permanent-magnet machine," *IEEE Trans. Magn.*, vol. 55, no. 7, Jul. 2019, Art. no. 8203906.
- Y. Shen and Q. Lu, "Overview of permanent magnet linear machines with primary excitation," *Trans. China Electrotechnical Soc.*, vol. 36, no. no. 11, pp. 2325–2343, Jun. 2021.
- Y. Shen, Q. Lu, H. Li, J. Cai, X. Huang, and Y. Fang, "Analysis of a novel double-sided yokeless multitooth linear switched-flux PM motor," *IEEE Trans. Ind. Electron.*, vol. 65, no. 2, pp. 1837–1845, Feb. 2018.
- Z. Zeng and Q. Lu, "A novel hybrid-excitation switched-flux linear machine with partitioned-excitations," *IEEE Trans. Magn.*, vol. 55, no. 12, Dec. 2019, Art. no. 7502204.
- Z. Zeng, Y. Shen, Q. Lu, B. Wu, D. Gerada, and C. Gerada, "Investigation of a partitioned-primary hybrid-excited flux-switching linear machine with dual-PM," *IEEE Trans. Ind. Appl.*, vol. 55, no. 4, pp. 3649–3659, Jul./Aug. 2019.
- Y. Shen, Z. Zeng, Q. Lu, and C. H. T. Lee, "Design and analysis of double-sided flux concentrated permanent magnet linear machine with saturation relieving effect," *IEEE Trans. Ind. Electron.*, vol. 70, no. 10, pp. 10442–10453, Oct. 2023.
- R. Cao, M. Cheng, C. C. Mi, and W. Hua, "Influence of leading design parameters on the force performance of a complementary and modular linear flux-switching permanent-magnet motor," *IEEE Trans. Ind. Electron.*, vol. 61, no. 5, pp. 2165–2175, May 2014.
- M. Lu and R. Cao, "A novel double-sided high temperature superconducting linear modular flux-switching motor," *IEEE Trans. Appl. Supercond.*, vol. 31, no. 5, Aug. 2021, Art. no. 5202905.
- W. Huang, W. Hua, F. Yin, F. Yu, and J. Qi, "Model predictive thrust force control of a linear flux-switching permanent magnet machine with voltage vectors selection and synthesis," *IEEE Trans. Ind. Electron.*, vol. 66, no. 6, pp. 4956–4967, Jun. 2019.
- W. Wang, Y. Feng, Y. Shi, M. Cheng, W. Hua, and Z. Wang, "Fault-tolerant control of primary permanent-magnet linear motors with single phase current sensor for Subway applications," *IEEE Trans. Power Electron.*, vol. 34, no. 11, pp. 10546–10556, Nov. 2019.

- [16] R. Cao, M. Cheng, C. Mi, W. Hua, and W. Zhao, "A linear doubly salient permanent-magnet motor with modular and complementary structure," *IEEE Trans. Magn.*, vol. 47, no. 12, pp. 4809–4821, Dec. 2011.
- [17] Y. Shen, Z. Zeng, Q. Lu, and L. Wu, "Design optimization and performance investigation of linear doubly salient slot permanent magnet machines," *IEEE Trans. Ind. Appl.*, vol. 55, no. 2, pp. 1524–1535, Mar./Apr. 2019.
- [18] Y. Gao, R. Qu, D. Li, J. Li, and G. Zhou, "Consequent-pole flux-reversal permanent-magnet machine for electric vehicle propulsion," *IEEE Trans. Appl. Supercond.*, vol. 26, no. 4, Jun. 2016, Art. no. 5200105.
- [19] Y. Gao, R. Qu, D. Li, J. Li, and L. Wu, "Design of three-phase flux-reversal machines with fractional-slot windings," *IEEE Trans. Ind. Appl.*, vol. 52, no. 4, pp. 2856–2864, Jul./Aug. 2016.
- [20] Y. Gao, R. Qu, D. Li, and J. Li, "Torque performance analysis of three-phase flux reversal machines," *IEEE Trans. Ind. Appl.*, vol. 53, no. 3, pp. 2110–2119, May/Jun. 2017.
- [21] H. Y. Li and Z. Q. Zhu, "Analysis of flux-reversal permanent-magnet machines with different consequent-pole PM topologies," *IEEE Trans. Magn.*, vol. 54, no. 11, Nov. 2018, Art. no. 8105305.
- [22] H. Li, Z. Q. Zhu, and H. Hua, "Comparative analysis of flux reversal permanent magnet machines with toroidal and concentrated windings," *IEEE Trans. Ind. Electron.*, vol. 67, no. 7, pp. 5278–5290, Jul. 2020.
- [23] H. Li and Z. Q. Zhu, "Influence of adjacent teeth magnet polarities on the performance of flux reversal permanent magnet machine," *IEEE Trans. Ind. Appl.*, vol. 55, no. 1, pp. 354–365, Jan./Feb. 2019.
- [24] H. Yang, H. Lin, Z. Q. Zhu, S. Lyu, and Y. Liu, "Design and analysis of novel asymmetric-stator-pole flux reversal PM machine," *IEEE Trans. Ind. Electron.*, vol. 67, no. 1, pp. 101–114, Jan. 2020.
- [25] H. Yang, Z. Q. Zhu, H. Lin, H. Li, and S. Lyu, "Analysis of consequent-pole flux reversal permanent magnet machine with biased flux modulation theory," *IEEE Trans. Ind. Electron.*, vol. 67, no. 3, pp. 2107–2121, Mar. 2020.
- [26] S. Chung, H. Lee, and S. Hwang, "A novel design of linear synchronous motor using FRM topology," *IEEE Trans. Magn.*, vol. 44, no. 6, pp. 1514–1517, Jun. 2008.
- [27] B. Kou, J. Luo, X. Yang, and L. Zhang, "Modeling and analysis of a novel transverse-flux flux-reversal linear motor for long-stroke application," *IEEE Trans. Ind. Electron.*, vol. 63, no. 10, pp. 6238–6248, Oct. 2016.
- [28] Y. Shen, T. Shi, Q. Lu, and C. Xia, "Robust design and analysis of asymmetric-excited flux reversal PM linear machine for long-stroke direct drive propulsion," *IEEE Trans. Magn.*, vol. 57, no. 6, Jun. 2021, Art. no. 8106104.
- [29] Y. Shen and Q. Lu, "Design and analysis of hybrid-excited flux modulated linear machines with zero-sequence current excitation," *IEEE J. Emerg. Sel. Topics Power Electron.*, vol. 10, no. 2, pp. 1834–1846, Apr. 2022.
- [30] Y. Shen, Q. Lu, and Y. Li, "Design criterion and analysis of hybrid-excited Vernier reluctance linear machine with slot Halbach PM arrays," *IEEE Trans. Ind. Electron.*, vol. 70, no. 5, pp. 5074–5084, May 2023.
- [31] Q. Lu, L. Wu, B. Wu, Y. Shen, Y. Li, and Z. Zhang, "Investigation of a novel linear partitioned primary hybrid-excited consequent-pole flux-reversal permanent magnet machine," *IEEE Trans. Ind. Appl.*, vol. 59, no. 2, pp. 1530–1540, Mar./Apr. 2023.
- [32] N. J. Baker, M. A. H. Raihan, A. A. Almoraya, J. W. Burchell, and M. A. Mueller, "Evaluating alternative linear Vernier hybrid machine topologies for integration into wave energy converters," *IEEE Trans. Energy Convers.*, vol. 33, no. 4, pp. 2007–2017, Dec. 2018.
- [33] W. Zhao, J. Zheng, J. Wang, G. Liu, J. Zhao, and Z. Fang, "Design and analysis of a linear permanent-magnet Vernier machine with improved force density," *IEEE Trans. Ind. Electron.*, vol. 63, no. 4, pp. 2072–2082, Apr. 2016.



Yiming Shen (Member, IEEE) received the B.Eng. and Ph.D. degrees in electrical engineering from the College of Electrical Engineering, Zhejiang University, Hangzhou, China, in 2015 and 2020, respectively.

He is currently a Research Fellow with the School of Electrical and Electronic Engineering, Nanyang Technological University, Singapore. His research interests include design and analysis of novel permanent magnet machines with particular reference to linear machines for direct drive applications.



Zhaokai Li (Member, IEEE) received the B.S. and Ph.D. degrees in electrical engineering from Zhejiang University, Hangzhou, China, in 2015 and 2020, respectively.

From 2018 to 2019, he was a Visiting Student with the University of Cambridge, Cambridge, U.K. From 2020 to 2022, he was a Postdoctoral Researcher with Zhejiang University. He was a Postdoctoral Research with the KTH Royal Institute of Technology, Stockholm, Sweden. Since September 2023, he has been a Guest Researcher with ABB Corporate Research, Västerås, Sweden. His interests include analytical models and iron loss analysis for permanent magnet motors.



Zhiqiang Zeng received the B.Eng. degree in electrical engineering from Qingdao University, Qingdao, China, in 2015, and Ph.D. degree in electrical engineering from Zhejiang University, Hangzhou, China, in 2020.

He is currently a Research Fellow with the School of Electrical and Electronic Engineering, Nanyang Technological University, Singapore. His research focuses on the design and analysis of novel permanent magnet machines.



Qinfen Lu (Senior Member, IEEE) received the B.Eng., M.Sc., and Ph.D. degrees in electrical engineering from Zhejiang University, Hangzhou, China, in 1996, 1999, and 2005, respectively.

Since 1999, she has been with the College of Electrical Engineering, Zhejiang University, where she is currently a Professor. Since 2019, she has also been a Part-Time Professor with the Lanzhou University of Technology, Lanzhou, China. Her research interests include analysis and control of linear machines and permanent magnet machines.



Christopher H. T. Lee (Senior Member, IEEE) received the B.Eng. and Ph.D. degrees in electrical engineering from the Department of Electrical and Electronic Engineering, The University of Hong Kong, Hong Kong, in 2009 and 2016, respectively.

He is currently an Assistant Professor with Nanyang Technological University, Singapore and an Honorary Assistant Professor with the University of Hong Kong. He was a Postdoctoral Fellow and then a Visiting Assistant Professor with the Massachusetts Institute of Technology, Cambridge, MA, USA. He has authored or coauthored one book, three books chapters, and more than 160 referred papers. His research interests include electric machines and drives, renewable energies, and electromechanical propulsion technologies.

Dr. Lee was the recipient of many awards, including MDPI Energies Young Investigator Award, NRF Fellowship, Nanyang Assistant Professorship, Li Ka Shing Prize (the best Ph.D. thesis prize), and Croucher Foundation Fellowship. He is an Associate Editor for IEEE TRANSACTIONS ON INDUSTRIAL ELECTRONICS, IEEE TRANSACTIONS ON ENERGY CONVERSION, IEEE ACCESS, and IET Renewable Power Generation. He is a Chartered Engineer in Hong Kong.